Article

TRANSPARENT PROCESS OPEN ACCESS

EMBO reports

A combinatorial panel for flow cytometry-based isolation of enteric nervous system cells from human intestine

Jonathan D Windster[1,2,†], Andrea Sacchetti[3,*,†], Gerben J Schaaf[2,4,5], Eric MJ Bindels[6], Robert MW Hofstra[2,‡], Rene MH Wijnen[1], Cornelius EJ Sloots[1] & Maria M Alves[2,**]

Abstract

Efficient isolation of neurons and glia from the human enteric nervous system (ENS) is challenging because of their rare and fragile nature. Here, we describe a staining panel to enrich ENS cells from the human intestine by fluorescence-activated cell sorting (FACS). We find that CD56/CD90/CD24 co-expression labels ENS cells with higher specificity and resolution than previous methods. Surprisingly, neuronal (CD24, TUBB3) and glial (SOX10) selective markers appear co-expressed by all ENS cells. We demonstrate that this contradictory staining pattern is mainly driven by neuronal fragments, either free or attached to glial cells, which are the most abundant cell types. Live neurons can be enriched by the highest CD24 and CD90 levels. By applying our protocol to isolate ENS cells for single-cell RNA sequencing, we show that these cells can be obtained with high quality, enabling interrogation of the human ENS transcriptome. Taken together, we present a selective FACS protocol that allows enrichment and discrimination of human ENS cells, opening up new avenues to study this complex system in health and disease.

Keywords ENS; enteric glia; enteric neurons; FACS; flow cytometry; human intestine

Subject Categories Methods & Resources

DOI 10.15252/embr.202255789 | Received 14 July 2022 | Revised 31 January 2023 | Accepted 10 February 2023 | Published online 28 February 2023

EMBO Reports (2023) 24: e55789

Introduction

The enteric nervous system (ENS) is located along the gastrointestinal (GI) tract and coordinates a variety of functions such as gut motility, nutrient absorption, and barrier defense (Furness, 2006). The human ENS comprises enteric neurons and enteric glial cells (EGCs) distributed within the myenteric and submucosal plexuses. Similar to the architecture of the central nervous system (CNS) in which neurons and glia are found in close contact with each other and with other cell types, ENS cells are tightly embedded within the surrounding tissue. Neuronal cell bodies are localized within ganglia between the muscle layers of the intestine. EGCs are present in almost every layer of the intestine, either closely packed together with neurons and their projections, or more dispersed within the lamina propria, where they interact with enterocytes, epithelial, and immune cells. However, despite being a relatively small compartment (it is estimated that enteric neurons are $< 0.01\%$ of total human colon cells; Graham *et al*, 2020), the ENS plays a key role in intestinal function. Its importance is highlighted by the wide range of enteric neuropathies that ensue when the development of the ENS is compromised. The most well-understood serious enteric neuropathy is Hirschsprung disease (HSCR), characterized by a lack of enteric neurons in a variable length of the intestine (Holschneider & Puri, 2008). There are also increasing data linking the ENS to other pathologies, such as irritable bowel disease, colorectal cancer, and neurodegenerative disorders (Holland *et al*, 2021). To understand ENS-specific pathologies, it is thus vital to have access to methodology allowing the study of ENS biology at the single-cell level.

Isolation of enteric neurons, glia, and their progenitors from the surrounding intestinal tissue has been an important goal in the field of enteric neurobiology (Bondurand *et al*, 2003; Metzger *et al*, 2009; Heanue & Pachnis, 2011). However, due to the localization and

[1] Department of Pediatric Surgery, Erasmus MC-Sophia Children's Hospital, Rotterdam, The Netherlands
[2] Department of Clinical Genetics, Erasmus University Medical Center, Sophia Children's Hospital, Rotterdam, The Netherlands
[3] Department of Pathology, Josephine Nefkens Institute, Erasmus Medical Center, Rotterdam, The Netherlands
[4] Department of Pediatrics, Erasmus University Medical Center, Sophia Children's Hospital, Rotterdam, The Netherlands
[5] Center for Lysosomal and Metabolic Diseases, Erasmus MC University Medical Center, Rotterdam, The Netherlands
[6] Department of Hematology, Erasmus MC Cancer Institute, Rotterdam, The Netherlands
*Corresponding author. Tel: +31107044490; E-mail: a.sacchetti@erasmusmc.nl
**Corresponding author. Tel: +31107030683; E-mail: m.alves@erasmusmc.nl
[†]These authors contributed equally to this work
[‡]Deceased

tightly packed arrangement of ENS cells, as well as their complex morphology and delicate constitution, it has proven difficult to isolate them from human intestinal tissue in sufficient purity and numbers. To date, methods for the isolation of ENS cells have primarily been based on enzymatic dissociation, in combination with culturing of dissociated cells in an ENS-favoring culture medium (Wilkinson *et al*, 2015; Cheng *et al*, 2017). Viable cells are then subjected to fluorescence-activated cell sorting (FACS) using specific cell surface markers. CD271 (Nerve Growth Factor Receptor (NGFR)) has been the most commonly used marker for the enrichment of ENS cells, despite it not being restricted to the ENS (Bixby *et al*, 2002; Sato & Heuckeroth, 2008). Although such protocols provide the ability to scale up ENS cell capture, culturing is known to induce dramatic changes in the transcriptome/epigenome of cells, which can subsequently introduce biases in the obtained results and mask disease-induced changes (Evans, 2015). Thus, methods that allow for faithfully capturing the *in-situ* cellular states of ENS cells are needed.

In the current study, we aimed to develop a highly specific FACS-based method to efficiently isolate ENS cells. To identify more selective and specific alternatives to CD271 that would allow such an approach, we have explored recent studies using single-cell and single-nuclei transcriptomics on the bulk of human intestinal cells (Drokhlyansky *et al*, 2020; Elmentaite *et al*, 2021; Fawkner-Corbett *et al*, 2021). Also, the available literature on ENS immunohistochemistry and flow cytometry was reviewed. Based on these data, CD56 (neural cell adhesion molecule 1 (NCAM1)) was found to be expressed on all ENS cells and to be very selective for them (Geramizadeh *et al*, 2013; Badizadegan *et al*, 2014; Rollo *et al*, 2015). CD90 (Thy-1), although not selective, was reported to be widely expressed in both neurons and glia (Bannerman *et al*, 1988; Bradley *et al*, 2009) and was a potential good counterstain to restrict our analysis to nonepithelial cells. Finally, CD24 (cluster of differentiation 24 or heat stable antigen) known for its expression in epithelial cells, was also reported as a marker of neuronal differentiation and was thus considered to be a good candidate for additional discrimination of neurons versus glial cells (Pruszak *et al*, 2009; Yuan *et al*, 2011). Here, based on the expression of these surface markers, CD56/CD90/CD24, we describe a new combinatorial panel capable of enriching and subdividing human ENS cells from intestinal material, rendering the investigation of these rare cell types from primary tissue accessible.

Results

CD56/CD90 co-expression distinguishes ENS cells from a heterogeneous pool of intestinal cell types and identifies two ENS subclusters

Based on literature and transcriptomic findings, we selected an initial extracellular antibody staining panel, which included CD56 and CD271 as putative ENS-selective markers (Hao & Young, 2009; Rollo *et al*, 2015, 2016; Drokhlyansky *et al*, 2020; Fawkner-Corbett *et al*, 2021). CD90 was added as a nonselective ENS inclusion marker, while CD45 and CD31 (for immune-hematopoietic and endothelial cells, here referred to as Lin^+), and EpCAM, a pan-epithelial marker (Litvinov *et al*, 1994), were added as exclusion markers. Finally, CD24 was also considered as neuron versus glia-selective marker. We first validated protein expression for CD56, CD90, and CD24 by immunostaining, in pediatric intestinal tissue sections. All markers showed expression in the ENS, co-localizing with both glial (S100B) and neuronal (ELAVL4) specific markers (Fig 1A). Using Collagenase II/Dispase, we prepared live single-cell suspensions from full-thickness human ileum samples. Preliminary steps in flow cytometric analysis such as exclusion of Lin^+ cells, as well as dead cells and other unwanted populations (e.g., small debris and multicellular aggregates), and the necessary isotype and compensation controls, are shown in Appendix Fig S1A–C. ENS cells were initially identified by co-expression of CD56 and CD271 (Fig 1B), which showed a very well-demarcated ENS cluster. Notably, while 97 ± 3% (mean ± SD) of $CD56^+$ cells were also $CD271^+$, variable proportions of $CD271^+$ cells (on average 37 ± 16% (mean ± SD)) were $CD56^-$ across experiments, suggesting that these cells could be non-ENS contaminants (Fig 1B–E, Appendix Fig S1D and E). CD90 and EpCAM showed the expected pattern, staining separate populations and demonstrating that ENS cells were $CD90^+$ and $EpCAM^-$ (Appendix Fig S1E). $CD56^+CD90^+$ cells showed complete overlap with the ENS cluster defined by CD56/CD271 co-expression (Fig 1D and E). The ENS cells identified following this strategy were on average 7.1 ± 4.2% (mean ± SD) of total Live/Lin^- cells with moderate variability between samples. Interestingly, while $CD56^+CD271^+$ identified a homogeneous ENS cluster, $CD56^+CD90^+$ cells appeared to be subdivided into two clusters, $CD90^L$ (CD90 left) and $CD90^R$ (CD90 right; Fig 1D). Although the gap between the two subclusters was minimal and full separation between them was challenging in most samples, this was a first step towards a subdivision of ENS cells, potentially allowing discrimination of neurons from glia.

By performing post-sorting reverse transcriptase quantitative PCR (RT–qPCR) for neuronal and glial markers, we confirmed that $CD56^+CD90^+$cells contained both neurons and glial cells (Fig 1F). An identical staining pattern of CD56/CD90 was observed in preparations from the human colon (Fig 1G). Further validation and dissection of the colonic ENS cluster were thus performed in parallel with ENS cells from the small intestine. Since no major differences were found between the two sections of the intestine, the confirmatory data relative to colon are mainly reported in Supplementary data. As CD271 staining had inferior discriminatory capacity and appeared redundant and unnecessary for ENS cell identification, from this point on, we decided to identify the ENS cluster as $CD56^+CD90^+$ and proceed to its further validation and characterization.

The ENS cluster consists of a mixed pool of free non-nucleated neuronal fragments and nucleated cells carrying neuronal fragments

In literature, ratios of neurons to glia present in the human intestine are not well established, especially in children. It is, however, predicted that in adult colon, glia outnumber neurons in the myenteric plexus in a ratio within ganglia of approximately 2–4:1 (Graham *et al*, 2020) and in the adult ileum of approximately 7:1 (Hoff *et al*, 2008). To gain insights into the proportions of neurons and glia that contribute to the $CD56^+CD90^+$ cluster in the pediatric ENS, we added to our panel the extracellular marker CD24 (neuron vs. glia-specific). This marker, although affected by inter-sample variations and sensitive to a number of experimental procedures (a few

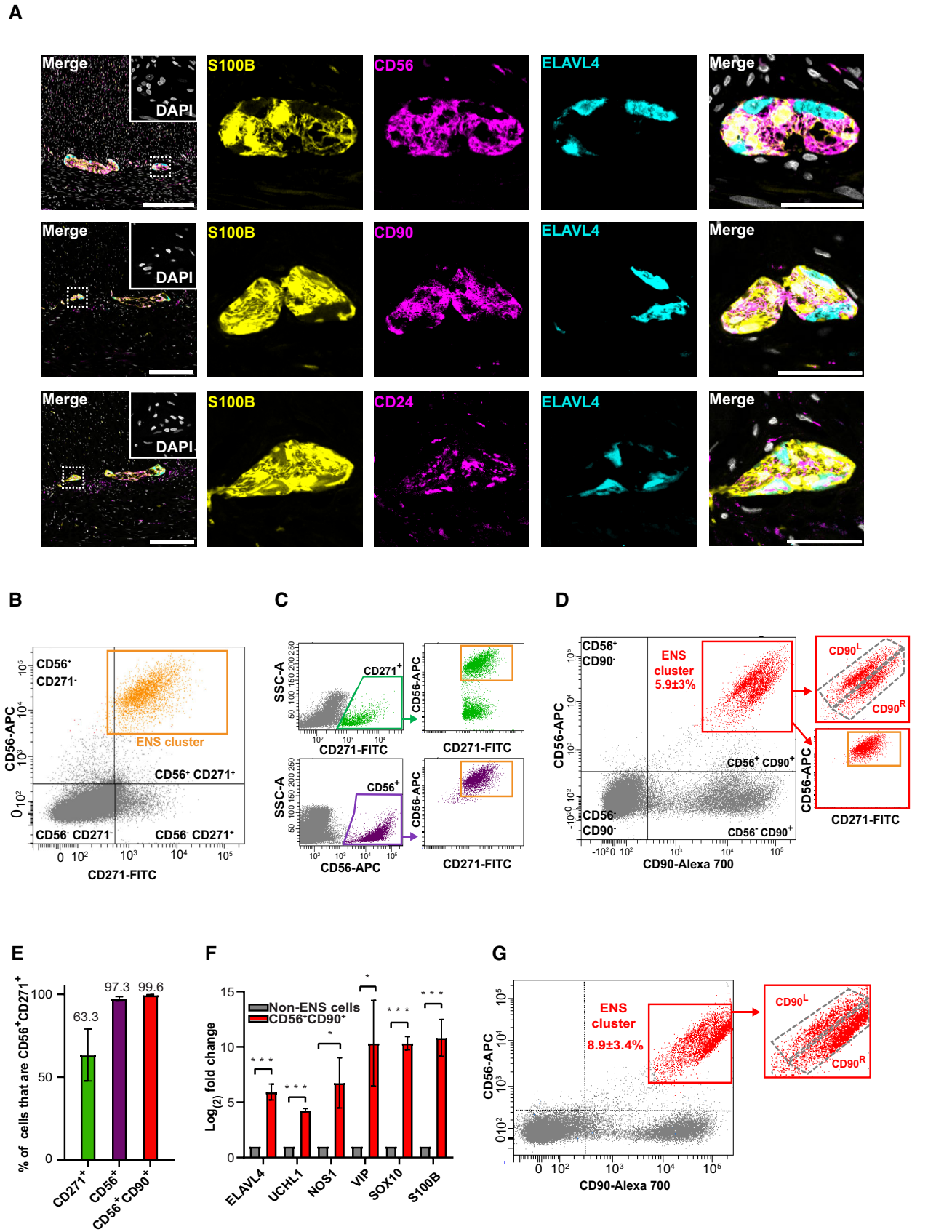

Figure 1.

Figure 1. Identification of the ENS cluster from pediatric intestinal material.

A Maximum intensity projections of the pediatric (0–12 months) small intestine showing the distribution of CD56, CD90, and CD24 within the ENS. The first image of each row shows a low-magnification overview and an inset depicting the DAPI channel in high magnification. The remaining panels correspond to the high magnification inset. Scale bar in overview images = 200 μm. Scale bar in high magnification panels = 40 μm.

B Initial identification of the ENS cluster as $CD56^{+}CD271^{+}$. ENS cells are in orange and non-ENS cells in gray. The ENS gate is outlined in orange.

C Gating on the single markers CD271 and CD56 (upper left and bottom left plot, respectively) versus SSC, followed by the analysis of the match of CD271 and CD56 single positive cells with the previously defined double positive $CD271^{+}CD56^{+}$ ENS cluster. CD56 shows a much better match than CD271.

D The ENS cluster identified as $CD56^{+}CD90^{+}$, highlighted in red to differentiate it from the $CD56^{+}CD271^{+}$ defined ENS cluster, shows two subpopulations here defined as $CD90^{R}$ and $CD90^{L}$ (upper inset) and has a complete match with the $CD271^{+}CD56^{+}$ cluster (lower inset). The average percentage (mean ± SD) of ENS cells in representative ileum preparations was 7.1 ± 4.2% (mean ± SD, $N = 20$ biological replicates).

E Histogram plot showing the percentage (mean ± SD, $N = 5$ biological replicates) of positive cells for the single markers CD271 and CD56, and $CD56^{+}CD90^{+}$, with the $CD56^{+}CD271^{+}$ cluster used in this initial phase, as "high purity standard".

F RT–qPCR from $CD56^{+}CD90^{+}$ sorted cells versus control non-ENS cells for representative neuronal and glial markers, confirms high enrichment of both neurons and glial cells (mean ± SD, $N = 4$ biological replicates, $^{*}P < 0.05$, $^{***}P < 0.001$, multiple Student's t-test, FDR correction for multiple comparisons).

G Single-cell preparations from the human colon show the same staining pattern observed in the small intestine and a comparable amount of ENS cells (8.9 ± 3.4%; mean ± SD, $N = 11$ biological replicates).

examples are provided in Appendix Fig S2A), stained the entire ENS cluster (Fig 2A, Appendix Fig S2A–E). Based on transcriptomic data (Drokhlyansky *et al*, 2020; Elmentaite *et al*, 2021; Fawkner-Corbett *et al*, 2021), CD24 was expected to be exclusive to neurons within the ENS cluster, and thus this staining pattern was unexpected. Interestingly, however, CD24 identified two major ENS subpopulations, here defined as $CD56^{+}CD24^{LOW}$ and $CD56^{+}CD24^{HI}$, which showed correspondence with the previously described $CD90^{L}$ and $CD90^{R}$ ENS subclusters, respectively (Fig 2A, Appendix Fig S2B–E). A perfect match between these populations was however difficult to obtain, due to the minimal gap and often-inevitable overlap between the CD90-based subpopulations. To further investigate these results, post-fixation staining with intracellular neuronal and glial-specific markers was performed. We used Tubulin Beta 3 (TUBB3) as neuronal selective, and SRY-Box Transcription factor 10 (SOX10), as glial selective markers. Expression of these markers had a nearly complete match with the $CD56^{+}CD90^{+}$ cluster (Fig 2B and C, Appendix Fig S2F–I). This confirmed that our ENS selection, based on extracellular markers, allowed for pure and exhaustive recovery of ENS cells, and also that $CD271^{+}CD56^{-}$ cells were not ENS cells. However, the co-expression of TUBB3 and SOX10 by the ENS cluster confirmed a major mismatch between the staining pattern and cell identity.

Neurons and glia are known to have an intricate physical relationship in all regions of the ENS. Therefore, we hypothesized that the co-expression of neuronal and glial markers on single cells could be a consequence of cellular fragments of neurons and glia remaining attached to each other and to other cells, even after enzymatic dissociation. To confirm this hypothesis, we first used DNA-binding cell-permeant dyes on live cells (nonpermeant dyes such as DAPI were used on fixed cells), to discriminate cellular debris from nucleated cells. We confirmed that the ENS cluster was made of nucleated cells, which were mainly in G0/G1 as expected, but also by non-nucleated particles of different sizes, appearing at different scattering levels (Fig 3A, Appendix Fig S3A). DNA staining also allowed refining single-cell gating, by removing the few doublets and clusters that escaped the previous FSC- and SSC-based single-cell gates, which were between 1 and 2% in live samples (Appendix Fig S3A and B). Moreover, selection for specific cell cycle phases (as G1/G0 for postmitotic ENS cells) could further exclude apoptotic cells (sub-G1 DNA content) and, eventually, cells above G1, such as proliferating (non-ENS) cells carrying some neural debris and minimal residual doublets. Notably, the non-nucleated neural particles showed largely overlapping staining and scattering patterns compared with the nucleated counterparts, although at a lower average intensity of these parameters (Fig 3B–D, Appendix Fig S3C–E). All the previously identified CD24- and CD90-based subclusters were present in both non-nucleated particles and nucleated cells, with only minor differences in the percentual distribution of the FACS events between subclusters (Fig S3C). This strongly suggested that the co-staining of neuronal (TUBB3, CD24) and glial markers (SOX10) was mainly dictated by the presence of neuronal fragments (axonal or dendritic) adhering to glial cells. Confocal microscopy on sorted ENS cells confirmed this hypothesis, allowing us to see that the vast majority of ENS cells showed 'patchy' bright $TUBB3^{+}CD24^{+}$ fragments attached to them, whereas a small minority of cells showed a more homogeneous $TUBB3^{+}CD24^{+}$ staining. The former were likely glial cells with neuronal fragments attached, while the latter were likely neurons (Fig 4A and B). Non-nucleated particles were confirmed to be totally DAPI-negative, thus validating our FACS selection of nucleated versus non-nucleated events, but showed a comparable expression of ENS markers as nucleated cells (Fig 4C).

Enteric neurons are characterized by the highest CD24 and CD90 expression

Although axonal or dendritic remnants could obscure the distinction between neurons and glia by flow cytometry analysis, the staining of soma or nuclear-specific neuronal markers should be capable of separating these populations. Among different candidates, we considered the use of NEUN, PHOX2B, and ELAVL4. However, NEUN, a good marker for neurons in the CNS, was only transcriptomically present on a subset of enteric neurons (Drokhlyansky *et al*, 2020), while the resolution of PHOX2B-staining was low due to low signal versus background ratio. ELAVL4 was able to identify a dimly positive population, which was 2.5 ± 1.1% (mean ± SD) of the nucleated ENS cells (Fig 5A). $ELAVL4^{+}$ cells localized on the tip of the $CD90^{R}$ ENS subcluster, and showed higher FSC/SSC compared with glial cells, suggesting larger cell size and higher granularity.

Taking advantage of the ELAVL4-based identification and of the subpopulations previously observed in the CD90/CD56 and CD24/CD56 plots, we tried to enrich neurons from live samples. With this

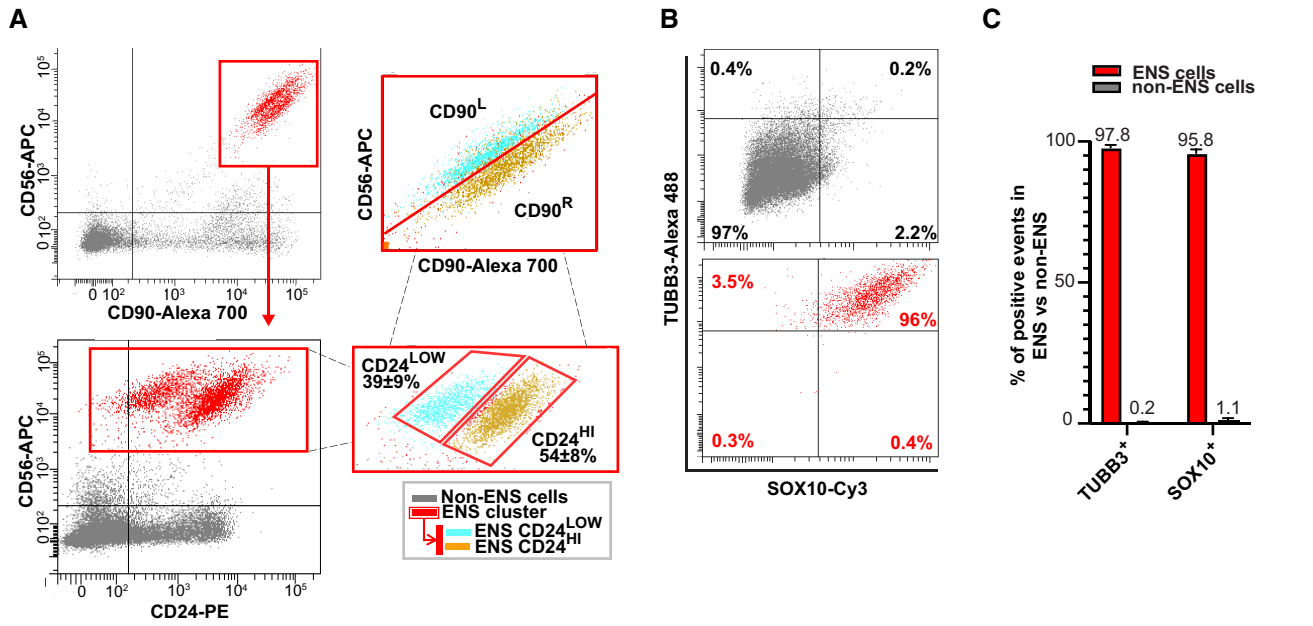

Figure 2. Further validation and subdivision of the ENS cluster.

A ENS cells from the human ileum, selected as $CD56^{+}CD90^{+}$ (upper left) are additionally stained for CD24 (bottom left). ENS cells are CD24+ (in optimal conditions $CD24^{+}$ ENS cells were 98 ± 1%, mean ± SD, $N = 8$ biological replicates) with evident subdivision in two main subpopulations, here defined $CD24^{LOW}$ and $CD24^{HI}$. Right lower inset: magnification of the ENS cells in a CD56/CD24 plot with the subpopulations labeled in cyan ($CD24^{LOW}$) and dark yellow ($CD24^{HI}$). The average percentage of $CD24^{LOW}$ and $CD24^{HI}$ is indicated inside the plot (mean ± SD of $N = 6$ biological replicates). Right upper inset: a magnification of the ENS cluster in a CD56/CD90 plot shows a good, although not perfect, match of $CD24^{LOW}$ (cyan) with $CD90^{L}$, and $CD24^{HI}$ (dark yellow) with $CD90^{R}$. For additional details and statistics see Appendix Fig S2B–E.

B Representative plot showing full co-expression of TUBB3 (neuronal marker) and SOX10 (glial marker), on ENS cells (bottom) and only minimal and low-intensity background on non-ENS cells (Top; $N = 1$ representative sample, for statistics, see Fig 2C). Intracellular staining was performed on formalin-fixed cells from the ileum, after prestaining for the extracellular markers. Selection of the ENS cluster in fixed cells is shown in Appendix Fig S2F.

C Percentage of $TUBB3^{+}$ and $SOX10^{+}$ cells in ENS and non-ENS cells (mean ± SD, TUBB3: $N = 4$ biological replicates, SOX10: $N = 3$ biological replicates). The single markers TUBB3 and SOX10 were gated versus SSC-A as shown in Appendix Fig S2G.

approach, we identified a small population at the tip of the $CD56^{+}CD24^{HI}$ cluster, which we defined as $CD24^{TIP}$. Consistently with previous ELAVL4-based localization, all the $CD24^{TIP}$ cells were on the tip of the $CD90^{R}$ subpopulation (Fig 5B). It should be noticed that while the $CD24^{TIP}$ appeared as a separate small population out of the $CD24^{HI}$ cluster, the same was not true with CD90 versus CD56, where a continuum of cells was observed on the tip of the $CD90^{R}$ cluster. As a consequence, not all the highest $CD90^{R}$ cells corresponded to the $CD24^{TIP}$, indicating lower discrimination and resolution in the CD90/CD56 plot.

RT–qPCR analysis on sorted $CD24^{TIP}$ ENS cells confirmed neuronal enrichment in this subpopulation versus all the remaining ENS cells, with a significant increase for *ELAVL4*, *SNAP25*, and *NOS1* (Fig 5C). Notably, the three populations ($CD24^{HI}$, $CD24^{LOW}$, and $CD24^{TIP}$) were also present in the non-nucleated fraction in similar proportion (Appendix Fig S4C), thus potentially indicating cell fragments associated with different neuronal (e.g soma, neurites, dendrites) and glial compartments. Additional validation of our neuronal enrichment strategy was done by comparing ganglionic versus aganglionic colon samples from pediatric patients with HSCR. In the aganglionic region of these patients, no neurons or very few of them are present and therefore, we expected the $CD24^{TIP}$ gate to be empty. Indeed, our results showed that while preparations from ganglionic colon had a neuronal population comparable to healthy intestines (approximately 3.1 ± 0.4% of the ENS cluster), in aganglionic colon, the neuronal fraction was essentially absent (Fig 5D and E, Appendix Fig S4E–J). Interestingly, also the subpopulation corresponding to $CD24^{LOW}$ was absent. Moreover, the same pattern, with a single $CD24^{HI}$ cluster, was again observed in both nucleated and non-nucleated events. Notably, total neural events were much higher in aganglionic tissue, 18.6 ± 7% versus 10 ± 3.6%, respectively (Appendix Fig S4I). Since aganglionic HSCR tissue is characterized by a strong compensative extrinsic innervation, the absence of the $CD24^{LOW}$ cluster most likely reflects the lack of dendrites or glial cells carrying dendrites, while the $CD24^{HI}$ cluster is likely to be composed of axonal debris of glia carrying axonal fragments.

Our protocol can be exploited for cell sorting of highly enriched neuronal and glial populations and subsequent gene expression analysis

As many downstream assays require an ample number of viable cells, we first verified whether our digestion protocol performed optimally in terms of ENS cell recovery and viability, while enriching for ENS cells and preserving antibody reactivity. Therefore, we decided to compare the Collagenase II/Dispase method described here, with two recently reported ENS dissociation protocols, based on Collagenase D or Liberase (Morarach *et al*, 2021; Ahrends *et al*, 2022). Our results

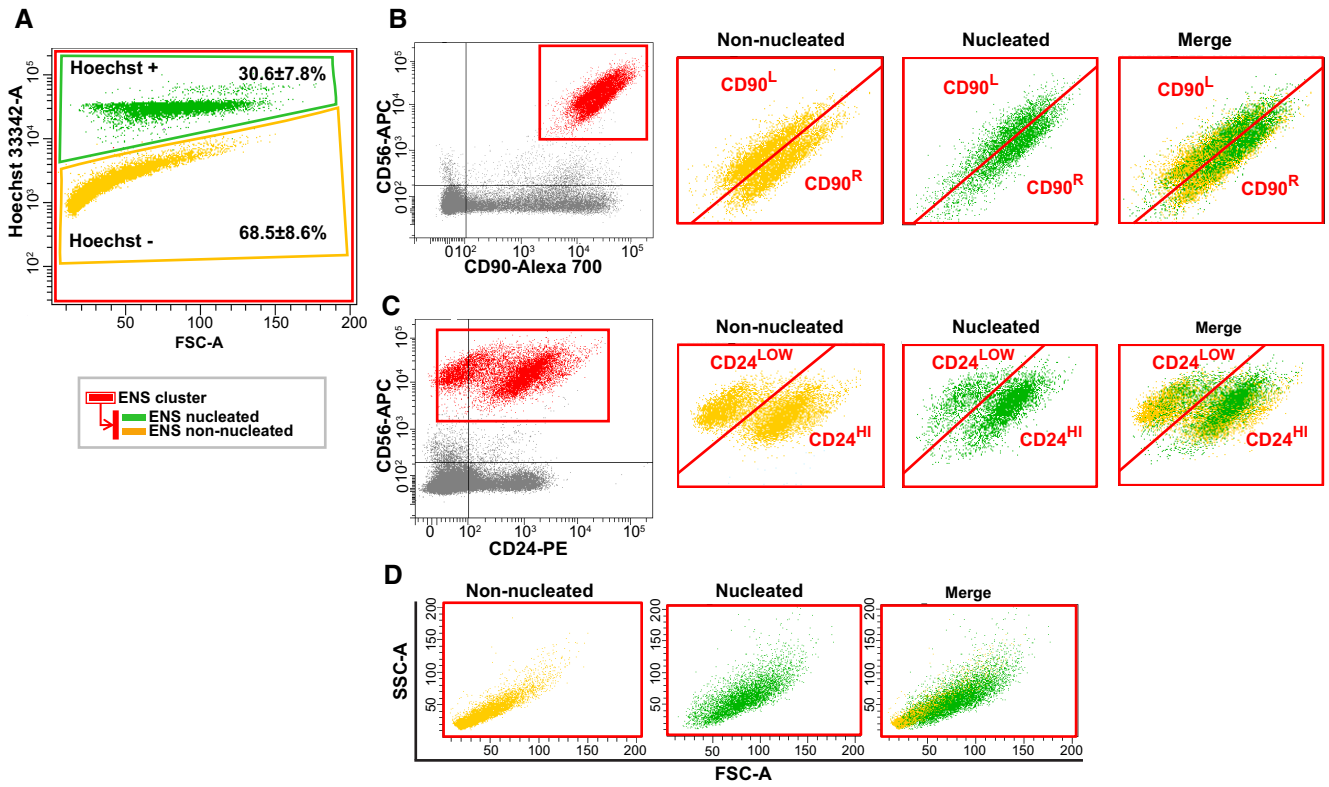

Figure 3. Live nuclear staining of the ENS cluster.

A Live human intestinal cells (ileum) previously bulk sorted as Live/Lin- (as shown in Appendix Fig S1A), are further stained with the cell-permeant and selective DNA-binding dye Hoechst 33342, and analyzed. Hoechst 33342 staining subdivides the ENS cluster into nucleated cells (30.6 ± 7.8%) and non-nucleated particles (68.5 ± 8.6%; mean ± SD, $N = 6$ biological replicates), largely overlapping in size (FSC-A). Cells can be further refined by means of stringent doublet exclusion and cell cycle analysis, as shown in Appendix Fig S3A.

B The distribution of ENS cells and non-nucleated particles are represented in a CD56/CD90 plot. Left: initial selection of ENS cells. Right: zoom on the ENS cluster, where ENS events are shown as non-nucleated, nucleated, or merge. For additional details and statistics see Appendix Fig S3E.

C ENS cells and non-nucleated particles are shown in a CD56/CD24 plot, as in Fig 3B. Nucleated and non-nucleated events largely overlap and define the same subclusters in CD56/CD24 and CD56/CD90 plots, although the average staining intensity of the three markers is lower for non-nucleated events. For additional details and statistics see Appendix Fig S3E.

D ENS cells and non-nucleated ENS particles are largely overlapping in an FSC-A versus SSC-A plot.

showed that the Liberase protocol was too harsh on the integrity of surface markers and therefore it was excluded from subsequent analyses (Appendix Fig S5A). While yielding comparable cell viability, the Collagenase II/Dispase protocol resulted in higher recovery of ENS cells compared with Collagenase D (Appendix Fig S5B) and was thus chosen as the digestion protocol of choice for our downstream assays. Assessment of post-sorting viability (re-analysis of sorted cells by FACS using DAPI, and manual trypan blue-based cell count), indicated that sorted ENS cells were still 86 ± 4% alive (mean ± SD, $N = 3$ biological replicates) according to the current definition of viability based on membrane integrity. Moreover, no additional DNA fragmentation was observed by live cell cycle analysis of sorted samples when compared with unsorted ones, thus excluding the presence of DAPI-negative apoptotic-like cells.

Following this preliminary validation, we tested the ability of our protocol to enrich $CD56^{+}CD90^{+}$ ENS cells from the pediatric intestine for single-cell RNA sequencing (scRNAseq) (Fig 6A, Table 2). For these experiments, we used four samples yielding an average of ~ 38,000 cells after sorting, of which 23,886 were successfully sequenced. Transcriptomic data confirmed high enrichment of ENS cells and showed the presence of 91.0 ± 5.1% (mean ± SD) glia and 7.4 ± 2.2% (mean ± SD) contaminant cells (Fig 6B). In good agreement with the proportion found by flow cytometry for $ELAVL4^{+}$ and $CD24^{TIP}$ cells, the neuronal population identified by scRNAseq, corresponded to 1.6 ± 0.7%. Dataset integration did not reveal gross differences in cluster contribution from small intestine versus colon samples (Fig 6C). Notably, the predicted sorting purity by FACS (≥ 99%) was higher than the one obtained by scRNAseq (≤ 93%), which was potentially due to non-ENS cells carrying bright neuronal terminations attached to them (e.g., synaptic fragments).

EGCs showed the expression of previously described canonical glial markers, such as *S100B*, *SOX10*, and *PLP1* and as expected, limited expression of *CD24* (Fig 6D and E). Enteric neurons clustered separately from EGCs in the UMAP embedding and showed expression of canonical neuronal markers, such as *ELAVL4*, *RET*, and *UCHL1*. In a subset analysis, the neuronal cluster partitioned into four main clusters, which we annotated as enteric differentiating neurons, enteric sensory neurons (ESN), enteric excitatory

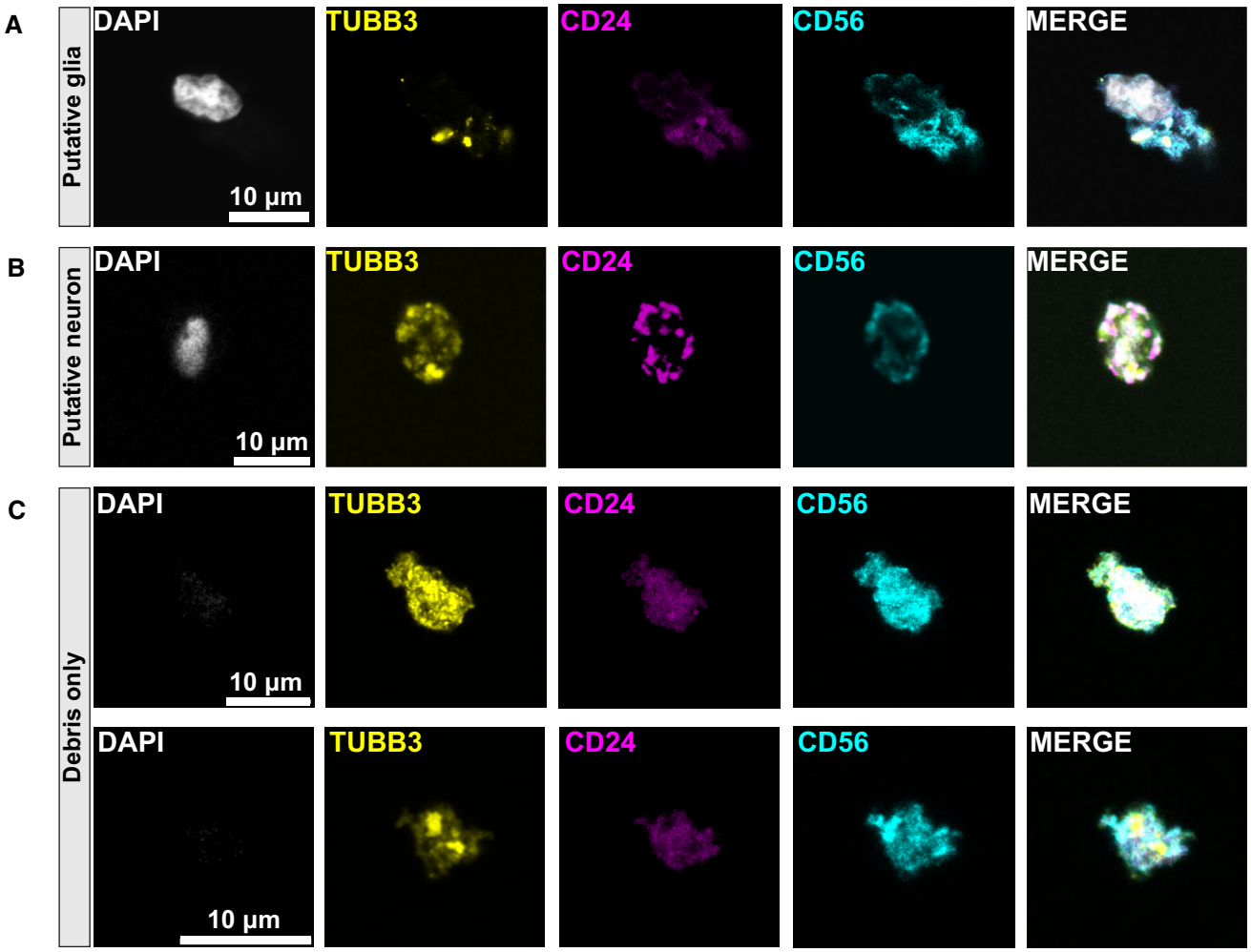

Figure 4. Microscopy of sorted ENS cells.

Confocal images of ENS events sorted as nucleated and non-nucleated, as shown in Fig 3.

A, B (A) Most of the staining belongs to what appears to be non-nucleated ($DAPI^-$) cellular debris (putative neuronal terminations) attached to a nucleated cell (putative glial cell). This is particularly true for TUBB3 and CD24, which show (as expected for neuronal selective markers) a starker distinction than CD56 (also expressed by glial cells). At a very low frequency among sorted ENS cells, we could observe putative neurons as represented in (B), with a more homogenous distribution of the three markers.

C Examples of sorted Hoechst-negative ENS debris, which are confirmed to be non-nucleated (thus validating our gates on Hoechst 33342-A) but positive for all neuronal markers.

motor neurons (EEMN), and enteric inhibitory motor neurons (EIMN; Fig 6F). The latter three clusters were characterized by markers matching major subsets of enteric neurons previously described (Jakob *et al*, 2021), with the expression of neurotransmitters such as *SST* (EPSN) and *NOS1* (EIMN), as well as chemokines such as *CXCL12* (EEMN; Fig 6G). Notably, differentiating neurons were enriched for various genes previously linked to enteric neural progenitor states such as *EDNRB* and *NOTCH1* (Okamura & Saga, 2008; Sasselli et al, 2012), while showing reduced expression of more differentiated neuronal markers, such as *SNAP25*. Additionally, this cluster was enriched for several extracellular matrix markers such as *COL21A1* and *COL4A5*, which have not yet been linked to ENS development.

Discussion

The tight and compact arrangement of the ENS, and the limited number of enteric neurons and glia in the gut, complicates the isolation of these fragile and morphologically complex cells, limiting their targeted examination. Moreover, an ENS-specific panel of markers for neurocytometry is currently lacking.

Based on recent transcriptomic studies as well as previous immunohistochemical and flow cytometry data of the ENS, we selected CD56, CD90, and CD24 as potential candidates to improve the enrichment of these cells from intestinal biopsies. Comparative analysis with CD271 showed considerable overlap of $CD271^+$ and $CD56^+$ cells, thereby defining a *bona fide* pure ENS cluster. However, while

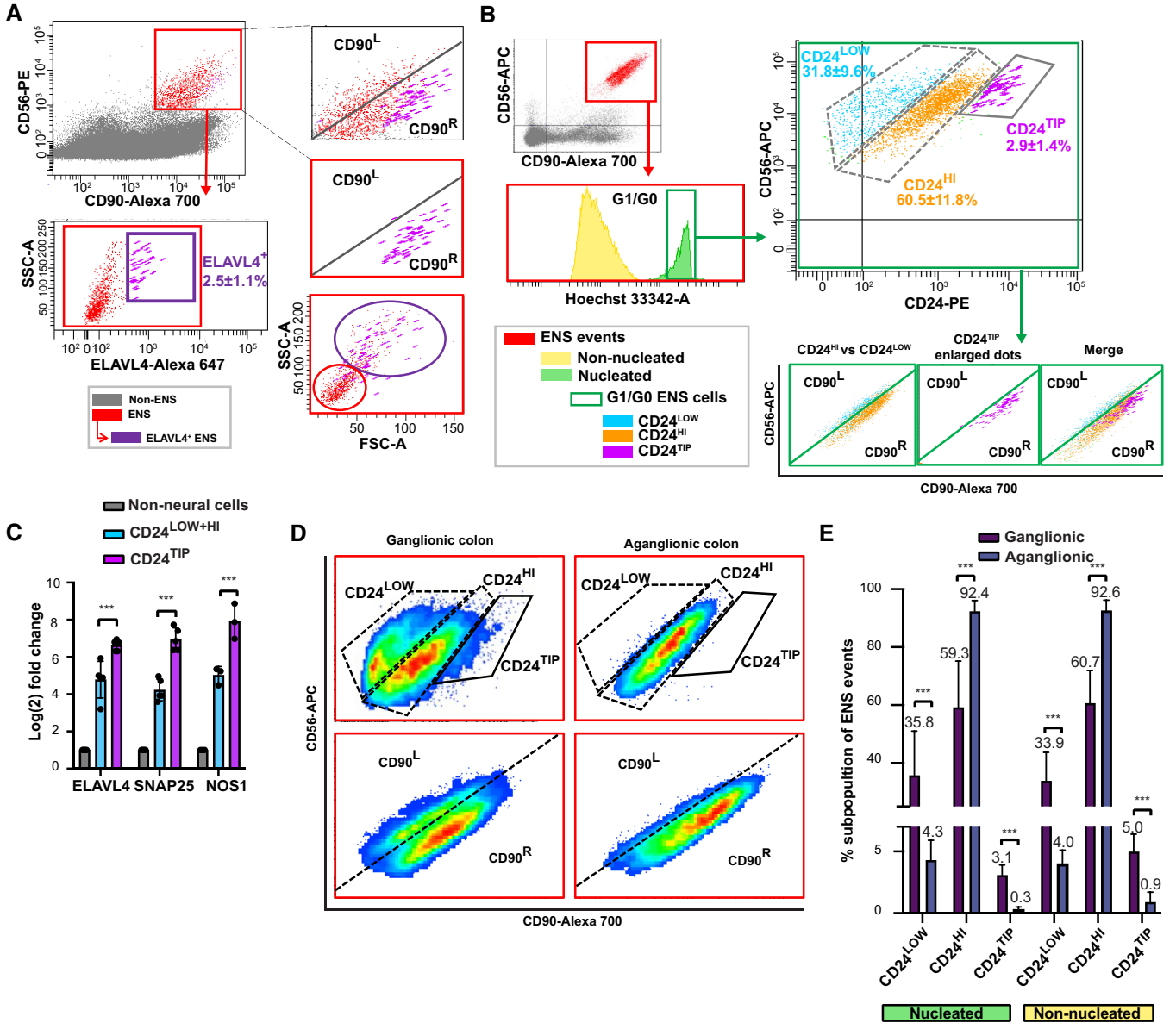

Figure 5. Discrimination of enteric neurons from EGCs.

A Upper left plot: selection of ENS cells as $CD56^{+}CD90^{+}$ in a methanol fixed sample from human ileum. The intensity of CD56 and CD90 (both stained before fixation) is much lower than in live cells but sufficient for ENS cell identification. Bottom left: ELAVL4 staining shows the presence of 2.5 ± 1.1% (mean ± SD, $N = 3$ biological replicates) $ELAVL4^{+}$ ENS cells (purple "large" dots according to FACS DIVA software). Dots were enlarged to improve visibility in small-size plots. Normal size dots are reported in Appendix Fig S4A for comparison. Right plots: $ELAVL4^{+}$ cells, as defined by SSC-A versus ELAVL4, correspond to the tip of the $CD90^{R}$ ENS subcluster in a CD56/CD90 plot. Upper right inset: all ENS cells are shown, and $CD24^{TIP}$ cells are highlighted in purple; middle-right inset: only $CD24^{TIP}$ cells are shown. Bottom right: an FSC-A versus SSC-A plot shows higher scattering-distribution of putative neurons versus glial cells.

B Selection of ENS cells in a live sample from human ileum, previously sorted as $Live/Lin^{-}$ (upper left plot), is followed by gating single nucleated cells in G0/G1 (bottom left plot). Upper right plot: among ENS cells in G1/G0, a small subpopulation is visible on the right tip of the CD24-based distribution, here defined as $CD24^{TIP}$ and highlighted in purple using again "large" dots for better visibility. Bottom right plots: zoom on ENS cells in a CD56/CD90 plot. $CD24^{TIP}$ cells are localized in the upper part of the $CD90^{R}$ ENS subcluster. The percentage of each CD24-based subpopulation is indicated in the CD24 versus CD90 plot as mean ± SD, $N = 6$ biological replicates. Further details are given in Appendix Fig S4B–D.

C RT–qPCR for neuronal markers on cells sorted for $CD24^{TIP}$ versus all the other ENS cells, confirms strong neuronal enrichment (mean ± SD, $N = 5$ biological replicates, $^{***}P < 0.001$, multiple Student's t-test, FDR correction for multiple comparisons).

D Comparison of an aganglionic (right) versus ganglionic colon (left) preparation from an HSCR patient (surgery was performed at the age of 4 months), using density plots that show all ENS events (cells + debris). A striking difference can be appreciated not only in the $CD24^{TIP}$, which is totally absent as expected, but also in the $CD24^{LOW}$ cluster. This cluster, which is also absent, is paralleled by a similar unbalance of the corresponding $CD90^{R}$ and $CD90^{L}$ subclusters.

E Graph showing the proportion of the CD24-based subclusters in the nucleated versus non-nucleated fraction of ganglionic and aganglionic colon (mean ± SD, $N = 4$ biological replicates, $^{***}P < 0.001$, multiple Student's t-test, FDR correction for multiple comparisons). Additional details and statistics are shown in Appendix Fig S4E–J.

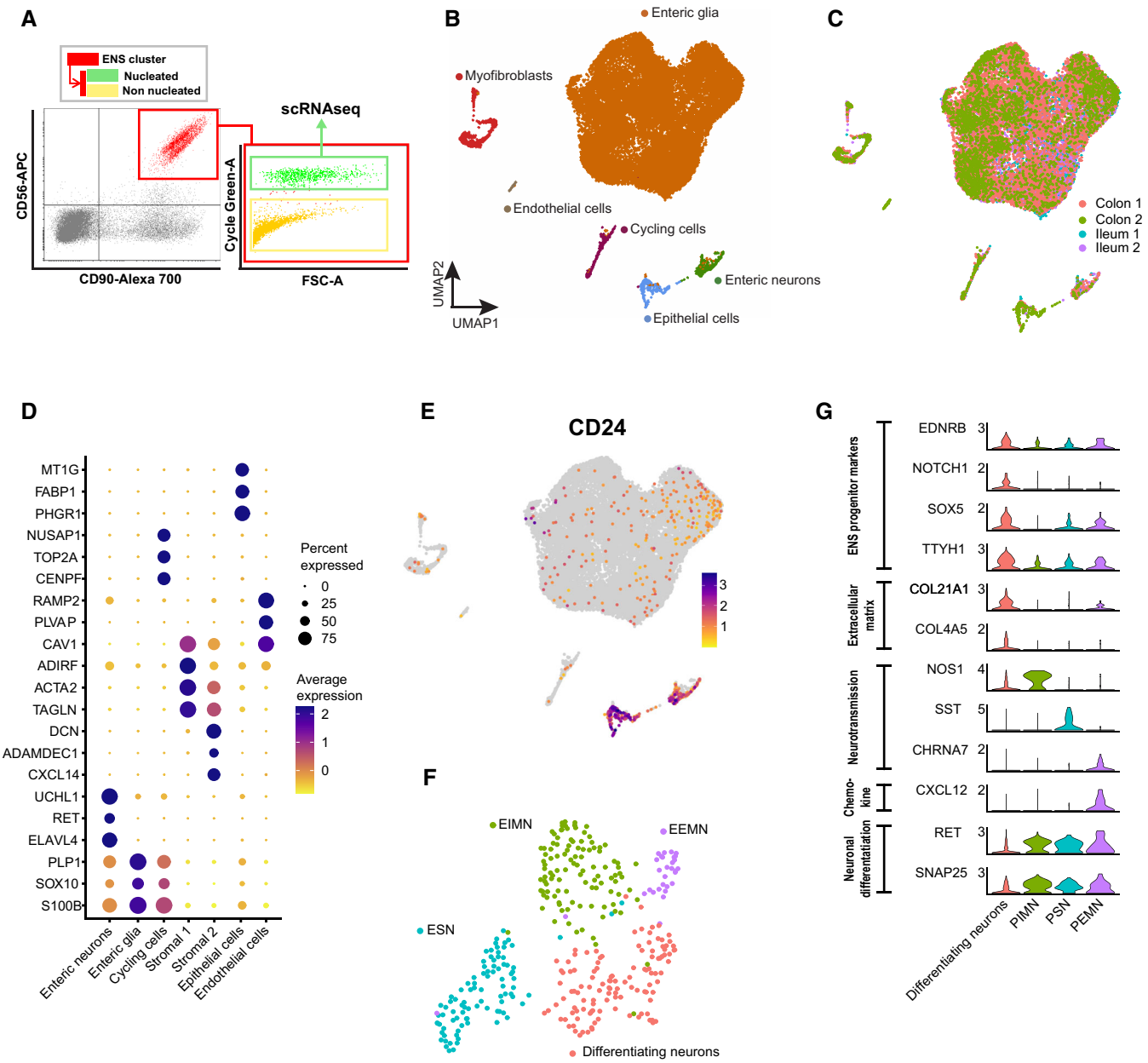

Figure 6. Characterization of sorted ENS cells by scRNAseq.

A Schematic representation of the sorting procedure for scRNAseq. Standard selection of Live/Lin$^-$/CD56$^+$CD90$^+$ ENS cluster cells was followed by the selection of nucleated events. Negative selection of DAPI- (live) and Lin$^-$ cells was performed as shown in Appendix Fig S1A. The procedure is as shown in Fig 3, with the difference that here nuclear staining was based on Cycle Green instead of Hoechst3342, and was performed in a single staining step. This is because the blue emitting viability dye DAPI (and also the Lin antibodies) allowed co-staining with the green emitting cell cycle dye Cycle Green.

B Uniform manifold approximation and projection (UMAP) of CD56$^+$CD90$^+$ sorted cells. The majority of captured cells are EGCs with minor contributions from contaminating cell types. Enteric neurons are also captured, albeit at a low frequency (1.6%).

C UMAP of CD56$^+$CD90$^+$ sorted cells colored by sample origin. Relatively equal contribution of cells is observed from both colonic and ileal samples to the individual clusters.

D Dot plot of top markers from each of the captured cell types. Each cell cluster can be defined by its own set of canonical markers.

E Expression of CD24 across the entire dataset shows the increased expression in neurons and epithelial cells, and limited expression in glia, as expected.

F UMAP of a subset of enteric neurons. Four subtypes of enteric neurons can be discerned.

G Stacked violin plots showing enriched genes in specific neuronal subtypes.

CD56 produced a bright CD56$^+$ cluster that had good concordance with CD271$^+$ cells, CD271 staining had inferior discriminatory capacity, also staining non-ENS cells. Combining CD90 with CD56 showed added value for ENS cell analysis, as it allowed the identification of two ENS subclusters. Moreover, CD90/CD56 co-staining allowed better discrimination of ENS cells over CD56 alone, in

particular in samples associated with a lower signal-to-noise ratio, which occurs particularly in fixed samples. In this context, CD271 appeared redundant for ENS cell identification and also not necessary in further steps of the subdivision of the ENS cluster.

Additional staining with the neuronal-specific marker CD24, as well as TUBB3 (neuronal marker) and SOX10 (glial marker), confirmed exhaustive and high-purity identification of ENS cells by means of our extracellular staining panel. However, all markers appeared to be co-expressed in cells that should selectively express either neuronal or glial markers. We hypothesized that the ambiguous staining pattern of the ENS cluster was mainly derived from the inevitable fragmentation of neuronal terminations during tissue digestion, which remained partially attached to glial cells, thus creating a mismatch between single-cell identity and staining pattern. Such phenomenon has been demonstrated previously in the CNS (Berl *et al*, 2017), but has but never been properly investigated or experimentally demonstrated in the gut. DNA staining revealed that indeed, the ENS cluster comprised a large proportion of non-nucleated neural particles with a similar expression of surface markers as nucleated cells. Confocal microscopy confirmed the presence of neuronal remnants (axonal/dendritic) attached to glial cells.

In an ultimate attempt to differentiate neurons from glia, we used the neuronal soma-specific marker ELAVL4, which, in fixed samples, localized neurons on the tip of the $CD90^{R}$ ENS subcluster. We hypothesized that neurons should also have the highest CD24 levels and indeed, we found a small population on the tip of the ENS cluster ($CD24^{TIP}$), which also appeared on the tip of the $CD90^{R}$ ENS subcluster, consistent with the previous localization of $ELAVL4^{+}$ ENS cells. The enrichment of neurons in the $CD24^{TIP}$ subcluster was confirmed by RT–qPCR. These results show, for the first time, that human enteric neurons can be discriminated from EGCs by FACS and is in line with previous data, showing that CD24 is a marker of neuronal differentiation in the CNS (Gilliam *et al*, 2017).

Although the goal of this study was not to perform a comprehensive comparison of dissociation methods, among the ones previously used for ENS single-cell preparations, we found that Collagenase II/Dispase provides a good compromise between dissociation efficiency, cell viability and preservation of surface markers for ENS cells. While comparative data on digestion methods for ENS isolation from the human gut are lacking, a comprehensive review on the murine intestine recently corroborated the use of Collagenase for this particular purpose (Schonkeren *et al*, 2021). Importantly, the method described herein is based on full-thickness intestinal biopsies, while the previous work has relied considerably on preparations in which the myenteric plexus was solely dissected and used for subsequent single-cell preparation (Grundmann *et al*, 2015; Zeisel *et al*, 2018; Huang *et al*, 2020; Wright *et al*, 2021). The latter procedure can result in a biased sampling of EGCs, which are known to be distributed across the entire gut wall axis, but also of enteric neurons present in the submucosa and adjacent to the epithelium (Seguella & Gulbransen, 2021).

As a validation of our protocol, we performed scRNAseq on sorted $CD56^{+}CD90^{+}$ ENS cells. The transcriptomic data obtained showed that our FACS panel is ENS-selective, with only limited contamination of other cell types. We presume that the minor contribution of non-ENS cell types to our sorted fractions is mostly due to a similar phenomenon as seen in our postsorting microscopy, namely the adherence of $CD56^{+}CD90^{+}$ ENS debris (such as synaptic fragments) to non-ENS cells. Regardless, with this approach, we were able to obtain a clear separation of enteric neurons and EGCs. This is likely explained by the fact that cell fragments are largely devoid of intact mRNA and therefore do not contribute to the sequencing data. Notably, neurons appeared at a much lower ratio versus glial cells (1:59) than expected (Hoff *et al*, 2008; Graham *et al*, 2020). It is important to note, however, that these quantifications have been based on intraganglionic glial numbers rather than the entire gut wall axis, while a plethora of glial cells is present within the muscularis, as well as in nerve fibers traversing the gut wall. It is also worth mentioning that to date, no estimation of the number of enteric neurons versus glial cells has been done for the pediatric ENS, as all studies reported have been performed using fetal or adult intestinal material. However, it remains plausible that the relatively harsh conditions required to dissociate postnatal human gut tissue, have a detrimental effect on the survival of neurons, as a result of their fragile morphology. Alternatively, neurons may not be completely dissociated and thus, discarded together with other multicellular clusters. Also, the lower neuronal recovery by scRNAseq (1.6%) compared with the average percentage of $CD24^{TIP}$ cells observed by FACS on total ENS cells (approximately 3%), may reflect some loss of neurons during postsorting processing, including cell death and other issues inherent to the scRNAseq technique. Nonetheless, our data show that relative to the total number of cells or nuclei sequenced, we were able to recover a higher number of neurons than previously reported (Drokhlyansky *et al*, 2020; Wright *et al*, 2021). Further improvement of neuronal recovery, if feasible, is beyond the scope of this work, and should be addressed by dedicated studies, taking advantage of the new tools of ENS analysis we have here provided.

This is to our knowledge the first study showing that human ENS cells can be selectively isolated by flow cytometry and directly used for subsequent analyses. Up until now single-cell/nuclei studies of the human ENS were reliant on sequencing considerable numbers of cells to obtain a sufficient number of enteric neurons and glia. This approach hampers the efficient capture of ENS cells, resulting in the need to sequence a high number of cells and consequently, in high costs. Our method dramatically reduces the sequencing throughput required to capture sizeable amounts of these cells, thereby making single-cell studies more accessible to the ENS community. Moreover, in contrast to single-nuclei sequencing, our method relies on the capture of intact ENS cells, thereby mitigating potential loss of cytoplasmic mRNA that, especially in the context of neurites, axons, and glial projections, might bias transcriptomic profiling. While we focused here on scRNAseq as downstream validation, our method could be extended to other types of downstream analyses, as well as direct multicolor analysis in standard multicolor flow cytometry (including functional assays by adding different types of probes), imaging flow cytometry, and mass cytometry. Moreover, examples of postsorting applications include microscopy, RT–qPCR, bulk RNA sequencing, epigenomic assays, metabolomics, and protein-based studies.

Taken together, we present here a new isolation method that allows very selective ENS cell identification and sorting, as well as the separation of enteric neuronal versus glial populations. At the same time, we show how misleading it can be to rely on surface markers for defining cell identity, especially when dealing with cell types that are morphologically complex and connected with each

other and/or with adjacent tissue compartments via cellular projections. As such, our findings and isolation protocol could be applied to other tissues, improving the study of neuronal and glial cells in and outside of the CNS.

Materials and Methods

Human tissue

Pediatric intestinal tissue was collected from resection specimens of patients who underwent surgery at the Pediatric Surgery Department of the Erasmus University Medical Center—Sophia Children's Hospital. Patients, aged between 1 month and 1 year, underwent surgery for ileostomy or colostomy reversal, following previous surgery due to necrotizing enterocolitis or anorectal malformations (Table 2). In the operating room, full-thickness tissue biopsies of approximately 2–3 cm^2 were taken from discarded tissue of resection specimens, placed in 25 ml of ice-cold PBS, and transported within 30 min to our laboratory. Next, the tissue was vigorously shaken for 10 s and the PBS was decanted. These washing steps were repeated until the tissue was macroscopically devoid of feces. Full-thickness gut biopsies were then minced thoroughly with a scalpel into small pieces of approximately 5 mm^2. Aliquots of 500 mg of minced tissue were stored in cryovials containing 1.5 ml Cryostor cell cryopreservation media (C2874, Sigma). Additionally, biopsies from HSCR patients undergoing transanal pull-through surgery at the age of 4 months, were obtained and sampled in a similar fashion at the proximal ganglionic side, as well as the distal aganglionic segment. Samples were stored at −80°C for later use. The institutional review board of the Erasmus Medical Center has approved this study (MEC-2022-0336).

Dissociation of human intestinal tissue

Cryopreserved tissue (500 mg) was rapidly thawed in a 37°C water bath, washed with ice-cold PBS, and placed in a gentleMACS C-tube (130-093-237, Miltenyi Biotec) with 5 ml of digestion solution [DMEM/F12 (11320-074, Gibco) containing 10 mM HEPES (15630106, Thermo Fisher), and 200 μg/ml DNase I (11284932001, Sigma)]. Collagenase II (3 mg/ml; 17101-015, Gibco) + Dispase (0.25 mg/ml; 17105-041, Gibco), Collagenase D (2.5 mg/ml; 11088858001, Roche) or Liberase TM (0.42 mg/ml; 5401119001, Roche) were also added to the digestion solution. Liquid stocks of HEPES (1 M) were stored at 4 degrees, while stocks of DNAse I (10 mg/ml) were kept at −20 degrees. Collagenase II, Dispase, and Collagenase D were freshly prepared from powder (stored at −20 degrees).

The gentleMACS C-tube was placed in the gentleMACS Octo Dissociator (130-095-937, Miltenyi Biotec) for 1 h (program 37C_h_TDK_1), and the tissue suspension was gently triturated 10 times with a 19G needle and syringe, followed by 10 times with a 22G needle until a homogeneous suspension was achieved. If an occlusion of the needle was detected, the clogged piece of tissue was removed with a wet wipe and discarded. The suspension was filtered through a 70 μm cell strainer (130-098-458, Miltenyi Biotec) and mixed 1:10 with HBSS buffer without Ca^{2+} Mg^{2+} (14175095, Life Technologies), and 2% Fetal Bovine Serum. Afterwards, cells were washed by pelleting using a swinging bucket precooled (4 degrees) rotor, at 540 RCF for 3 min, with maximum acceleration and deceleration. The cell pellet was then resuspended in Red Blood Cell Lysis Solution (170-080-033, Miltenyi Biotec), as per the manufacturer's protocol. Cells were then centrifuged at 4 degrees, 540 RCF for 3 min, resuspended in 1 ml HBSS without Ca^{2+} Mg^{2+} and 2% Fetal Bovine Serum, and counted using an automated cell counter (BioRad).

Extra and intracellular staining

Antibodies used for intra- and extracellular surface antigens, as well as secondary antibodies, are listed in Table 1. Briefly, antibody staining was performed on ice for 30 min, in HBSS with 2% FBS. For dead cell exclusion during FACS analysis, cells were resuspended in 100 μl of HBSS with 2% FBS, pelleted twice and subsequently resuspended in HBSS with 2% FBS + DAPI (1 μg/ml; D9542, Sigma-Aldrich). For intracellular staining, cells were first stained live for cell surface markers and then incubated for 10 min with a LIVE/DEAD fixable viability dye at room temperature (RT) as per the manufacturer's protocol (130-109-816, Miltenyi Biotech). Subsequent fixation in 4% paraformaldehyde at RT (10′), double wash, and permeabilization with 0.2% PBS-Triton X-100 (15′, RT), were performed. Cells were then stained with intracellular markers in PBS, with 0.2% Triton X-100 and 1% BSA. For conjugated markers, cells were stained on ice for 90 min, subsequently washed using 1 ml PBS with 2% FBS and centrifuged at 4 degrees, 540 RCF for 3 min, followed by resuspension in 100 μl PBS. For unconjugated markers, cells were stained on ice with primary antibodies for 90 min in 100 μl PBS, subsequently washed using 1 ml PBS with 2% FBS and centrifuged at 4 degrees, 540 RCF for 3 min. Cells were then resuspended in 100 μl of PBS and stained for 1 h on ice with secondary antibodies. Afterwards, cells were washed with 1 ml PBS with 2% FBS, centrifuged as described above, and resuspended in 100 μl of PBS.

Immunofluorescence

Immunofluorescence was performed on tissues which were age-matched to our flow cytometry samples. Formaline fixed paraffin embedded (FFPE) tissue or fresh frozen samples which were embedded in optimal cutting temperature, were used. For FFPE material, 6 micron sections were deparaffinized in xylene and rehydrated in a graded ethanol series. Antigen retrieval was performed for 15 min at 94–96 °C on a hot plate in 10mM sodium citrate at pH 6. Antigen retrieval was performed in a similar fashion for frozen sections (6 micron) for 5 min. Primary antibodies were diluted in PBS and sections were incubated for 1.5 h. Sections were washed in PBS and incubated for 1 h with secondary antibodies. Sections were washed and mounted using Vectashield Vibrance Antifade Mounting Medium with DAPI (Vectorlabs, H1800-10). Images were taken on a Leica Stellaris 5 confocal laser scanning microscope with the 20x objective. Antibodies used are listed in Table 1.

Flow cytometry

Fluorescence-activated cell sorting analysis and sorting were performed with a BD FACS Aria III (BD Biosciences, New Jersey,

Table 1. FACS settings and reagents.

BD FACS Aria III Settings					
Flow cell	square				
Nozzle	85 or 100 micron				
Fluorophore	**Lasers**	**BP filter**	**LP filter**		
Hoechst/DAPI/BV421	405 nm	450/40			
FITC/Alexa 488/DyeCycle Green	488 nm	430/30			
PE/Cy3	561 nm	582/15			
APC/Cy5/Sytox Red	633 nm	660/20			
PerCPCy5.5	488 nm	695/40	655		
Alexa 700	633 nm	730/35	690		
List of primary antibodies used					
Antigen	**Reactivity**	**Fluorochrome**	**Company**	**Cat. #**	**Dilutions**
CD271	Human	FITC	Miltenyi Biotech	130-113-982	1:50
CD56	Human	APC	Biolegend	362504	1:20
CD56	Human	Unconjugated	Cell Signaling	99746T	1:100
CD90	Human	Alexa 700	Sony	2240600	1:20
CD90	Human	Unconjugated	Atlas Antibodies	AMAb90846	1:500
CD24	Human	PE	Biolegend	560991	1:10
CD24	Human	FITC	Miltenyi Biotec	130-112-844	1:50
CD31	Human	BV421	Biolegend	564089	1:20
CD45	Human	BV421	Biolegend	304031	1:20
EpCAM	Human	FITC	GeneTex	GTX30708	1:50
TUBB3	Human, Mouse	Alexa 488	Abcam	ab195879	1:100
TUBB3	Human	Biotin	Biolegend	801211	1:100
TUBB3	Human	Unconjugated	GeneTex	GTX130245	1:100
SOX10	Human, Mouse	Unconjugated	Cell Signaling Tech	89356S	1:100
S100β	Human	Unconjugated	Abcam	ab52642	1:200
ELAVL4	Human	Unconjugated	Molecular Probes	A-21271	1:50
ELAVL4	Human	Alexa 647	Santa Cruz Biotechnology	sc-48421	1:20
List of secondary antibodies					
Fab anti-mouse	Alexa 647	Jackson Immuno	715-607-003		1:250
Fab anti-mouse	Alexa 488	Jackson Immuno	715-547-003		1:250
Anti-rabbit	PE	Cell Signaling Tech	79408S		1:250
Streptavidin	FITC	Biolegend	405201		1:250
List of viability and cell cycle dyes					
		Company	**Cat. #**		
DAPI	–	Sigma	D9542-5MG		
Hoechst 33342	–	Sigma	B2261-100MG		
Viability Dye	–	Miltenyi Biotech	130-109-816		1:100
Vybrant DyeCycle Green		Invitrogen	V35004		1:100
List of primers pairs					
Primer	**Sequence**				
ELAVL4 F	CCCAGAAGGAACTGGAGCAACT				
ELAVL R	CCTTTGATGGCTTCTTCTGCCTC				
UCHL1 F	CCTGAAGACAGA CA AAATGC				
UCHL1 R	CCTGAAGACAGAGCAAAATGC				

Table 1 (continued)

BD FACS Aria III Settings	
NOS1 F	ACACGCATGTCTGGAAAGGCAC
NOS1 R	CTCTGTGGCATAGAGGATGGTC
VIP F	CCAGTCAAACGTCACTCAGATGC
VIP R	CTGGAAAGTCGGGAGATTCTCC
SNAP25 F	GGACGAACGGGAGCA ATG
SNAP25 R	CGCTCACCTGCTCTAGGTTTC
SOX10 F	AACGCCTTCATGGTGTGG
SOX10 R	CTTTCTTGTGCTGCATACGG
S100B F	ATTCTGGAAGGGAGGGAGAC
S100B R	TCCACAACCTCCTGCTCTTT
Actin F	AACCGCGAGAAGATGACCC
Actin R	GCCAGAGGCGTACAGGGATAG
GAPDH F	ATGGGGAAGGTGAAGGTCG
GAPDH R	TAAAAGCAGCCCTGGTGACC

Table 2. Pediatric intestinal samples used for scRNAseq.

Sample ID	Sex	Age at surgery (months)	Indication for surgery	Bowel region	Macroscopic examination	Weight of tissue (mg)	Cells sorted	Cells captured (10× Chromium Controller)
01	Male	3	Ileostomy closure after necrotizing enterocolitis	ileum	Healthy noninflamed tissue	~ 500	20.000	4.608
02	Male	2	Ileostomy closure after necrotizing enterocolitis	ileum	Healthy noninflamed tissue	~ 500	65.000	4.777
03	Male	5	Colostomy closure after anorectal malformation repair	Descending colon	Healthy noninflamed tissue	~ 500	44.000	9.922
04	Male	4	Colostomy closure after anorectal malformation repair	Descending colon	Healthy noninflamed tissue	~ 500	25.700	4.579

USA), using the parameters listed in Table 1. All samples were preliminarily gated by size and granularity, using a Side Scatter (SSC-A) versus Forward Scatter (FSC-A) plot, where A refers to the total area of the scattering signal produced, and results from the integration of the curve produced by H (height of the signal on Y) and W (width or length in time of the signal on X) to gate out the biggest aggregates and very small debris. Doublets were excluded using FSC-A versus FSC-W and SSC-A versus SSC-W gating (Roth *et al*, 2012; Huizer *et al*, 2017). This gating strategy ensured the inclusion of neurons with high FSC/SSC intensity and small-sized glial subpopulations (with low FSC/SSC signal intensity). Stringent and accurate single-cell gating was only applied on nuclear DNA staining (Appendix Fig S3A and B). Dead cells were excluded by means of the viability dyes described above, plotted against FSC-A. Lin^+ cells, here defined by CD31 and CD45 staining (identifying cells belonging to the immune-hematopoietic and endothelial cell lineages), were gated out together with dead cells in the same channel, thus keeping other channels free for additional markers. For the initial setup, fluorescence minus one (FMO) and isotype controls, were used for each antibody. Since all the fluorescent parameters referred to antibody staining where plotted as area (A) of the fluorescent signal, "A" is generally omitted in most of our FACS plots. Thus, FITC-A, APC-A, Alexa 700-A, and PE-A are simply indicated as FITC, APC, Alexa 700, and PE. However, we have kept the separate use of Hoechst-A and Hoechst-W since these parameters were used in combination, for doublet exclusion. Concerning fluorescent emission of ENS cells according to different markers, for the sake of simplicity we have omitted the definition of fluorescent levels, and used a simple "+" or "−," with the exception of cases where multiple clusters were detected and had to be differentiated, as with CD24

ENS cells (subdivided in $CD24^{HI}$, $CD24^{LOW}$, $CD24^{TIP}$) and CD90 (subdivided in Left and Right). However, all gates were mainly based on visible clusters, not on simple positivity for a marker. For example, CD56 was always "high" in live samples and low in some fixed samples but was universally indicated as $CD56^{+}$.

Gene expression analysis

RNA from $CD56^{+}CD90^{+}$-, $CD24^{LOW}CD24^{HI}$-, and $CD24^{TIP}$-sorted cells, was isolated using the RNeasy Plus Micro Kit (74034, Qiagen), according to the user manual. RT–qPCR was performed and relative expression was quantified using the $2^{-\Delta\Delta Ct}$ method, after normalization to actin and GAPDH. Experiments were performed in triplicate. Primers used are listed in Table 1.

Single-cell RNA sequencing and analysis

For scRNAseq, four control patients were analyzed (Table 2). One frozen vial containing approximately 500 mg of minced full-thickness intestinal biopsy, was used per patient. After tissue dissociation, cells were stained for CD56/CD90/CD24/Lin/DAPI and cycle green. $Live/Lin^{-}/CycleGreen^{+}/CD56^{+}CD90^{+}$ cells were sorted and concentrated in 25 µl of PBS. Subsequently the samples underwent droplet-based scRNAseq, using the 10× Chromium single-cell platform (10× Genomics, 3′ v3 chemistry), following the Single Cell 3′ Reagents Kits (v2) user guide (manual part no. CG00052, Rev D). Finalized libraries were sequenced on a Novaseq6000 platform (Illumina). Reads were aligned to the human genome GRCh38-3.0.0 and gene count processing was performed using CellRanger V.2.1.1 and V6.1. The R package Seurat v.4.0.0 was used to filter out doublets and low-quality cells (> 25% mitochondrial counts, unique feature counts over 6,000 or < 200, or total UMI over 30,000). We computed a ModuleScore using a curated set of genes upregulated during dissociation of tissue into single cells and regressed out the dissociation score, as well as the proportion of mitochondrial gene counts. We performed log-normalization of read counts and dimensionality reduction, based on principle component analysis. Cells were then clustered using Louvain algorithm for modularity optimization and k-nearest neighbors (KNN) graph as input. The two ileum and two colon datasets were integrated after performing batch correction using Seurat's FindIntegrationAnchor function. This yielded a total of 22,549 high-quality cells, of which 20,750 were EGCs and 351 were enteric neurons. Highly variable genes were identified, and clusters were annotated based on top markers. Figures were rendered using the scCustomize package (Marsh, 2021).

Statistical analysis

Data were tested for normality, using the Shapiro–Wilk test. If data passed this test either as nontransformed or log-transformed values, differences were analyzed using multiple unpaired Student's *t*-tests. The Mann–Whitney *U* test was used if data were not normally distributed. Data are presented as means with standard deviations. A $P < 0.05$ was considered to be significant. Statistical analyses were performed using GraphPad Prism version 9 (Graphpad Software®, La Jolla, CA, USA). All authors had access to the study data and reviewed and approved the final manuscript.

Data availability

The raw and processed single-cell data used for this study were deposited in NCBIs Gene Expression Omnibus and are accessible throught GEO Series accession number GSE224252 (https://www.ncbi.nlm.nih.gov/geo/query/acc.cgi?acc=GSE224252). The source code for the scRNAseq analysis for this study has been deposited on a public GitHub repository (https://github.com/jondawi/pediatric-scRNAseq).

Expanded View for this article is available online.

Acknowledgements

We would like to thank R.M. Hoogenboezem (Department of Hematology, Erasmus Medical Center) for processing our raw single-cell data and M.P. Verhagen (Department of Pathology, Erasmus Medical Center) for fruitful discussions and bio-informatic assistance. This work was supported by a grant from the Stichting Sophia Kinderziekenhuis Fonds to MMA and RMWH (S17-18).

Author contributions

Jonathan D Windster: Conceptualization; data curation; formal analysis; validation; investigation; visualization; methodology; writing – original draft; project administration; writing – review and editing. **Andrea Sacchetti:** Conceptualization; resources; data curation; formal analysis; supervision; visualization; methodology; writing – original draft; writing – review and editing. **Gerben J Schaaf:** Conceptualization; visualization; writing – review and editing. **Eric M J Bindels:** Investigation; methodology. **Robert M W Hofstra:** Conceptualization; resources; supervision. **Rene M H Wijnen:** Conceptualization; resources; supervision; writing – review and editing. **Cornelius E J Sloots:** Conceptualization; supervision; writing – review and editing. **Maria M Alves:** Conceptualization; resources; supervision; methodology; project administration; writing – review and editing.

Disclosure and competing interests statement

The authors declare that they have no conflict of interest.

References

Ahrends T, Weiner M, Mucida D (2022) Isolation of myenteric and submucosal plexus from mouse gastrointestinal tract and subsequent flow cytometry and immunofluorescence. *STAR Protoc* 3: 101157

Badizadegan K, Thomas AR, Nagy N, Ndishabandi D, Miller SA, Alessandrini A, Belkind-Gerson J, Goldstein AM (2014) Presence of intramucosal neuroglial cells in normal and aganglionic human colon. *Am J Physiol Gastrointest Liver Physiol* 307: G1002 – G1012

Bannerman PG, Mirsky R, Jessen KR (1988) Antigenic markers and laminin expression in cultured enteric neural cells. *Brain Res* 440: 87 – 98

Berl S, Karram K, Scheller A, Jungblut M, Kirchhoff F, Waisman A (2017) Enrichment and isolation of neurons from adult mouse brain for *ex vivo* analysis. *J Neurosci Methods* 283: 15 – 22

Bixby S, Kruger GM, Mosher JT, Joseph NM, Morrison SJ (2002) Cell-intrinsic differences between stem cells from different regions of the peripheral nervous system regulate the generation of neural diversity. *Neuron* 35: 643 – 656

Bondurand N, Natarajan D, Thapar N, Atkins C, Pachnis V (2003) Neuron and glia generating progenitors of the mammalian enteric nervous system isolated from foetal and postnatal gut cultures. *Development* 130: 6387 – 6400

Bradley JE, Ramirez G, Hagood JS (2009) Roles and regulation of Thy-1, a context-dependent modulator of cell phenotype. *Biofactors* 35: 258 – 265

Cheng LS, Hotta R, Graham HK, Belkind-Gerson J, Nagy N, Goldstein AM (2017) Postnatal human enteric neuronal progenitors can migrate, differentiate, and proliferate in embryonic and postnatal aganglionic gut environments. *Pediatr Res* 81: 838 – 846

Drokhlyansky E, Smillie CS, Van Wittenberghe N, Ericsson M, Griffin GK, Eraslan G, Dionne D, Cuoco MS, Goder-Reiser MN, Sharova T *et al* (2020) The human and mouse enteric nervous system at single-cell resolution. *Cell* 182: 1606 – 1622

Elmentaite R, Kumasaka N, Roberts K, Fleming A, Dann E, King HW, Kleshchevnikov V, Dabrowska M, Pritchard S, Bolt L *et al* (2021) Cells of the human intestinal tract mapped across space and time. *Nature* 597: 250 – 255

Evans TG (2015) Considerations for the use of transcriptomics in identifying the 'genes that matter' for environmental adaptation. *J Exp Biol* 218: 1925 – 1935

Fawkner-Corbett D, Antanaviciute A, Parikh K, Jagielowicz M, Geros AS, Gupta T, Ashley N, Khamis D, Fowler D, Morrissey E *et al* (2021) Spatiotemporal analysis of human intestinal development at single-cell resolution. *Cell* 184: 810 – 826

Furness JB (2006) *The enteric nervous system*. Oxford: Blackwell Publishing

Geramizadeh B, Akbarzadeh E, Izadi B, Foroutan H-R, Heidari T (2013) Immunohistochemical study of enteric nervous system in hirschsprung's disease and intestinal neuronal dysplasia. *Histol Histopathol* 28: 345 – 351

Gilliam DT, Menon V, Bretz NP, Pruszak J (2017) The CD24 surface antigen in neural development and disease. *Neurobiol Dis* 99: 133 – 144

Graham KD, Lopez SH, Sengupta R, Shenoy A, Schneider S, Wright CM, Feldman M, Furth E, Valdivieso F, Lemke A *et al* (2020) Robust, 3-dimensional visualization of human colon enteric nervous system without tissue sectioning. *Gastroenterology* 158: 2221 – 2235

Grundmann D, Klotz M, Rabe H, Glanemann M, Schafer KH (2015) Isolation of high-purity myenteric plexus from adult human and mouse gastrointestinal tract. *Sci Rep* 5: 9226

Hao MM, Young HM (2009) Development of enteric neuron diversity. *J Cell Mol Med* 13: 1193 – 1210

Heanue TA, Pachnis V (2011) Prospective identification and isolation of enteric nervous system progenitors using Sox2. *Stem Cells* 29: 128 – 140

Hoff S, Zeller F, von Weyhern CW, Wegner M, Schemann M, Michel K, Ruhl A (2008) Quantitative assessment of glial cells in the human and Guinea pig enteric nervous system with an anti-Sox8/9/10 antibody. *J Comp Neurol* 509: 356 – 371

Holland AM, Bon-Frauches AC, Keszthelyi D, Melotte V, Boesmans W (2021) The enteric nervous system in gastrointestinal disease etiology. *Cell Mol Life Sci* 78: 4713 – 4733

Holschneider AM, Puri P (2008) *Hirschsprung's disease and allied disorders*. Berlin Heidelberg: Springer

Huang Z, Liao L, Wang Z, Lu Y, Yan W, Cao H, Tan B (2020) An efficient approach for wholemount preparation of the myenteric plexus of rat colon. *J Neurosci Methods* 348: 109012

Huizer K, Mustafa DAM, Spelt JC, Kros JM, Sacchetti A (2017) Improving the characterization of endothelial progenitor cell subsets by an optimized FACS protocol. *PLoS One* 12: e0184895

Jakob MO, Kofoed-Branzk M, Deshpande D, Murugan S, Klose CSN (2021) An integrated view on neuronal subsets in the peripheral nervous system and their role in immunoregulation. *Front Immunol* 12: 679055

Litvinov SV, Velders MP, Bakker HA, Fleuren GJ, Warnaar SO (1994) Ep-CAM: a human epithelial antigen is a homophilic cell-cell adhesion molecule. *J Cell Biol* 125: 437 – 446

Marsh S (2021) scCustomize: an R package for custom visualization & analyses of single cell sequencing.

Metzger M, Bareiss PM, Danker T, Wagner S, Hennenlotter J, Guenther E, Obermayr F, Stenzl A, Koenigsrainer A, Skutella T *et al* (2009) Expansion and differentiation of neural progenitors derived from the human adult enteric nervous system. *Gastroenterology* 137: 2063 – 2073

Morarach K, Mikhailova A, Knoflach V, Memic F, Kumar R, Li W, Ernfors P, Marklund U (2021) Diversification of molecularly defined myenteric neuron classes revealed by single-cell RNA sequencing. *Nat Neurosci* 24: 34 – 46

Okamura Y, Saga Y (2008) Notch signaling is required for the maintenance of enteric neural crest progenitors. *Development* 135: 3555 – 3565

Pruszak J, Ludwig W, Blak A, Alavian K, Isacson O (2009) CD15, CD24, and CD29 define a surface biomarker code for neural lineage differentiation of stem cells. *Stem Cells* 27: 2928 – 2940

Rollo BN, Zhang D, Simkin JE, Menheniott TR, Newgreen DF (2015) Why are enteric ganglia so small? Role of differential adhesion of enteric neurons and enteric neural crest cells. *F1000Res* 4: 113

Rollo BN, Zhang D, Stamp LA, Menheniott TR, Stathopoulos L, Denham M, Dottori M, King SK, Hutson JM, Newgreen DF (2016) Enteric neural cells from Hirschsprung disease patients form ganglia in autologous Aneuronal colon. *Cell Mol Gastroenterol Hepatol* 2: 92 – 109

Roth S, Franken P, Sacchetti A, Kremer A, Anderson K, Sansom O, Fodde R (2012) Paneth cells in intestinal homeostasis and tissue injury. *PLoS One* 7: e38965

Sasselli V, Pachnis V, Burns AJ (2012) The enteric nervous system. *Dev Biol* 366: 64 – 73

Sato Y, Heuckeroth RO (2008) Retinoic acid regulates murine enteric nervous system precursor proliferation, enhances neuronal precursor differentiation, and reduces neurite growth in vitro. *Dev Biol* 320: 185 – 198

Schonkeren SL, Kuthe TT, Idris M, Bon-Frauches AC, Boesmans W, Melotte V (2021) The gut brain in a dish: murine primary enteric nervous system cell cultures. *Neurogastroenterol Motil* 34: e14215

Seguella L, Gulbransen BD (2021) Enteric glial biology, intercellular signalling and roles in gastrointestinal disease. *Nat Rev Gastroenterol Hepatol* 18: 571 – 587

Wilkinson DJ, Bethell GS, Shukla R, Kenny SE, Edgar DH (2015) Isolation of enteric nervous system progenitor cells from the Aganglionic gut of patients with Hirschsprung's disease. *PLoS One* 10: e0125724

Wright CM, Schneider S, Smith-Edwards KM, Mafra F, Leembruggen AJL, Gonzalez MV, Kothakapa DR, Anderson JB, Maguire BA, Gao T *et al* (2021) scRNA-sequencing reveals new enteric nervous system roles for GDNF, NRTN, and TBX3. *Cell Mol Gastroenterol Hepatol* 11: 1548 – 1592

Yuan SH, Martin J, Elia J, Flippin J, Paramban RI, Hefferan MP, Vidal JG, Mu Y, Killian RL, Israel MA *et al* (2011) Cell-surface marker signatures for the isolation of neural stem cells, glia and neurons derived from human pluripotent stem cells. *PLoS One* 6: e17540

Zeisel A, Hochgerner H, Lonnerberg P, Johnsson A, Memic F, van der Zwan J, Haring M, Braun E, Borm LE, La Manno G *et al* (2018) Molecular architecture of the mouse nervous system. *Cell* 174: 999 – 1014